Blocking and Frontogenesis by Two-Dimensional Terrain in Baroclinic Flow. Part II: Analysis of Flow Stagnation Mechanisms

STEPHEN T. GARNER

NOAA/Geophysical Fluid Dynamics Laboratory, Princeton, New Jersey

(Manuscript received 24 January 1997, in final form 9 June 1998)

ABSTRACT

Numerical solutions presented in a companion paper show that two-dimensional mesoscale terrain becomes a much stronger barrier to a continuously stratified flow when the flow contains warm advection. Here it is shown that this baroclinic enhancement is a strictly nonlinear phenomenon. The linear analysis indicates a weakening of the upstream response in warm advection. However, a weakly nonlinear analysis shows that baroclinicity facilitates blocking in warm advection by strengthening the nonlinearity in the cross-mountain momentum equation in such a way as to amplify the vertical shear on the windward flank of the ridge. This is enough to send the flow past the blocking threshold even when conditions over the mountain are too linear to produce wave breaking. A more intuitive mechanism whereby the upstream static stability is increased by the nonlinearity in the temperature equation is found to be much less important.

1. Introduction

A companion paper (Garner 1999, hereafter Part I) investigates the possibility that ''regional'' atmospheric fronts like the ones on the east coasts of North America and Asia could be a type of upstream influence by the coastal mountain ranges. It was found that baroclinicity in the form of a cross-mountain temperature gradient had a strong impact on the blocking effect of an idealized ridge if the relatively warm air is upstream. In that case, surface stagnation occurs for lower mountains and stronger winds than in the absence of warm advection. Here we wish to uncover the main reasons for the baroclinic effect.

As in Part I, we idealize the blocking problem by assuming a Boussinesq atmosphere with uniform stratification in the vertical and horizontal, a constant Coriolis parameter, and two-dimensional topography. In the limit of hydrostatic and incompressible flow, the response to the topography is then entirely determined by a Froude number (Fr), a Rossby number (Ro), and a nondimensional parameter measuring the baroclinicity. We define the first two as

$$\mathrm{Fr} = Nh_0/u_0 \quad \text{and} \tag{1}$$

$$\mathrm{Ro} = u_0/(fl_0), \tag{2}$$

where h_0 and l_0 are the height and width of the mountain ridge, respectively, N is the undisturbed buoyancy frequency, and f is the Coriolis parameter. The problem is linear in the limit of small Fr and quasigeostrophic in the limit of small Ro.

The third parameter is defined as

$$\beta = \Lambda/N, \tag{3}$$

where Λ is the vertical shear of the basic flow parallel to the ridge: $\overline{v}(z) = \Lambda z$. The basic-state Richardson number is thus $\mathrm{Ri} = 1/\beta^2$. The basic potential temperature varies linearly in x (across the mountain) in accordance with thermal wind balance. Warm advection implies $\beta < 0$ and cold advection corresponds to $\beta > 0$. In the two-dimensional framework, the cross-mountain temperature gradient does not alter the stability of the linear waves or introduce critical layers.

We can establish immediately whether the known barrier enhancement due to warm advection at finite amplitude (see Part I) is also present in linear solutions. In Fig. 1, the steady, cross-mountain surface wind anomaly is plotted as a function of distance from the mountain for $\beta = 0$ and ± 0.6. These results are produced by the numerical model used in Part I. The mountain has a Gaussian profile with a nondimensional halfwidth of $\mathrm{Ro}^{-1} = 0.5$. Linear results, obtained by running the model to steady state with $\mathrm{Fr} = 0.02$, are shown in Fig. 1a, and nonlinear results, with $\mathrm{Fr} = 1.0$, appear in Fig. 1b. Since the velocity is normalized by Nh_0, the differences between these two sets of results are entirely due to the nonlinearity. The nonlinear solution shows the expected baroclinic enhancement. However, at small amplitude, warm advection *weakens* the upstream dis-

Corresponding author address: Dr. Stephen T. Garner, NOAA/GFDL, Princeton University, P.O. Box 308, Princeton, NJ 08542.
E-mail: stg@gfdl.gov

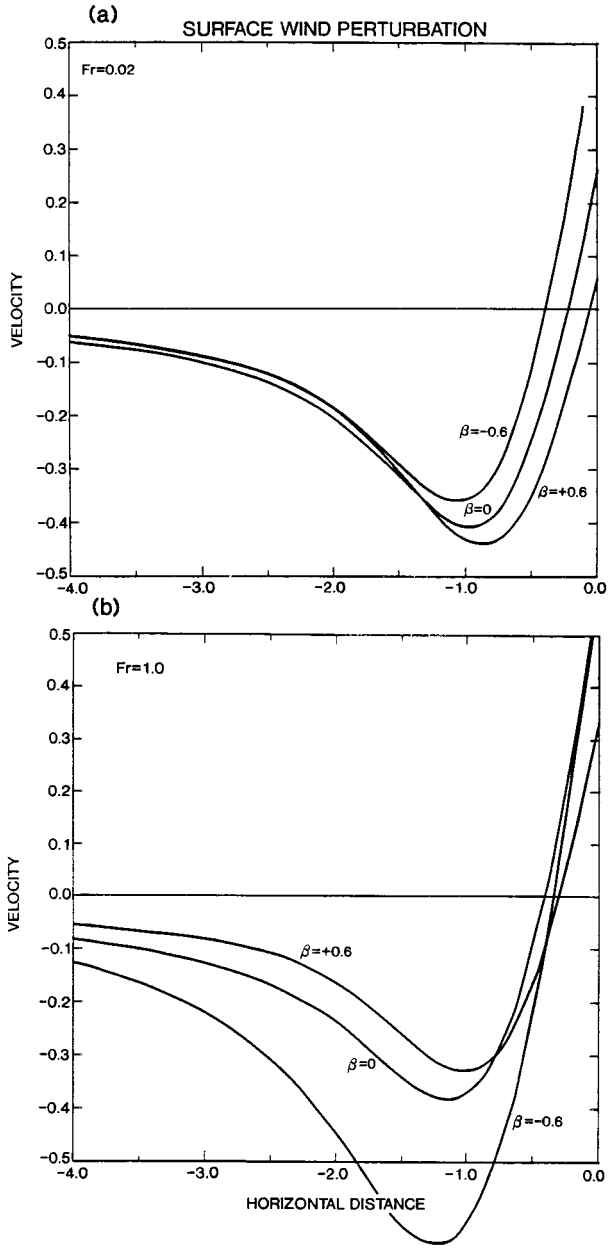

FIG. 1. Perturbation horizontal surface velocity u'_s in units of Nh_0 as a function of distance from the mountain for Ro = 2.0, three different values of β, and (a) Fr = 0.02 and (b) Fr = 1.0. Horizontal distance is in units of u_0/f.

turbance while cold advection strengthens it. Further experiments show this to be true at all values of Ro. Thus, the blocking enhancement due to warm advection first appears at finite amplitude.

To make analysis of the finite-amplitude problem tractable, we will rely on the ''weakly nonlinear'' assumption that the nonlinearity is given entirely by the linear solution. For context, it should be noted that the theory of weakly nonlinear solitary waves (e.g., Segur 1973) depends on a solvability condition to remove any projection of the nonlinearity onto the linear modes. This device is not available when the shape and amplitude of the waves are fixed by external (e.g., topographic) forcing. Something like the present approach was used by McIntyre (1972) in an analytical study of ducted, nonrotating, internal gravity modes. A related method used in Lighthill's (1952) analysis of jet noise and in Ley and Peltier's (1978) study of wave generation through frontal collapse attempts to extend the analysis into the strongly nonlinear regime by assuming that the nonlinearity is localized in space.

In their numerical study of mountain circulations in a barotropic atmosphere, Pierrehumbert and Wyman (1985) argue that even solutions that are nonlinear enough to have upstream influence (permanent inflow modification) may behave linearly far upstream because of the long horizontal scales and low intrinsic frequencies of the ''columnar'' disturbance. However, since stationary gravity–inertia waves are dispersive in the vertical, a weakly nonlinear solution for continuously stratified flow cannot show an unattenuated upstream disturbance of any amplitude. True upstream influence requires the systematic enlargement or intensification of the nonlinearity. There is a well-known far-field singularity in the linear response to single-signed distributions of terrain slope (Lilly and Klemp 1977) or heating (Bretherton 1988) that may suggest a more complete way to understand upstream influence in a dispersive medium. The present application places a weaker demand on the analysis because baroclinic blocking does not involve true upstream influence: the disturbance is always confined in the upstream direction, according to numerical solutions.

Weak nonlinearity due to the lower boundary condition has already been studied by Smith (1977) in the nonrotating limit. His analysis accounts for the steepening of stationary waves at periodic levels above the mountain. Experimental evidence was given by Garner (1995) that wave steepening and wave breaking are not directly important for upstream influence. Although that study excludes background rotation, it gives us some confidence that the effect of the remaining nonlinearity may be analyzed separately. Further confidence will come from direct comparisons to the nonlinear model solutions.

The plan is first to analyze the linear sensitivity of the steady solutions to baroclinicity and then to consider the weakly nonlinear modification, particularly as it is affected by the horizontal temperature stratification. In so doing, we will continue to focus on the case Ro = 2, which falls in the ''mesoscale'' range. In the nonrotating limit, far-upstream nonlinear effects cannot be understood from steady, linear solutions because *stationary*, hydrostatic gravity modes have no self-interaction (Long 1953; McIntyre 1972; Smith 1977) and no streamwise energy propagation. At finite Ro, however, stationary modes are self-interacting. Furthermore, baroclinicity allows streamwise energy propagation at some

hydrostatic scales. The transient nonlinearity and the weakly nonlinear response to it will also be considered, but more briefly.

2. Linear analysis

We start by scaling the Boussinesq system used in Part I. For disturbances containing a strong component of gravity–inertia waves, it is appropriate to use $(u^*, v^*) = Nh_0(u, v)$ and $w^* = fh_0 w$ for the perturbation velocity, and $x^* = (u_0/f)x$ and $z^* = (u_0/N)z$ for distance. Potential buoyancy will be scaled according to $b^* = (N^2 h_0)b$, and time according to $t^* = f^{-1}t$. The asterisk denotes the dimensional variable. By ignoring the $O(\mathrm{Fr})$ terms in the equations of Part I, we get the linearized, two-dimensional system

$$u_t + u_x = v_a + F^{(u)} \tag{4}$$

$$v_t + v_x = -\beta w - u + F^{(v)} \tag{5}$$

$$b_t + b_x = -\beta u - w + F^{(b)}, \tag{6}$$

where $F^{(u,v)}$ and $F^{(b)}$ refer to frictional and thermal forcing, respectively. All variables are departures from the uniformly stratified basic state. The subscript a refers to the ageostrophic part of the velocity, for example, $v_a = v - v_g$. The assumed y invariance of the velocity implies that u is entirely ageostrophic, or $u = u_a$.

For convenience, we assume hydrostatic balance,

$$(v_g)_z - b_x = 0, \tag{7}$$

and restrict attention to the incompressible case,

$$u_x + w_z = 0. \tag{8}$$

The mass streamfunction ψ satisfies $\psi_x = w$ and $\psi_z = -u$. The boundary conditions are $w = dh/dx$ at $z = 0$ and upward radiation or boundedness at $z = \infty$.

Note that β is the only parameter in (6)–(8). The height and width of the mountain enter via the lower boundary condition. Thus, $h = O(\mathrm{Fr})$ and $w = O(\mathrm{Ro})$. We are primarily interested in narrow mountains, with Ro of order unity or larger. The present scaling of the horizontal velocity is based on this limit, so that $u = O(1)$ at large Ro. The velocity in the most of the figures of Part I is normalized by u_0, which yields $u \sim \mathrm{Fr}$ at large Ro.

Steady, homogeneous solutions of (4)–(8) satisfy

$$\left(\frac{\partial^4}{\partial x^2 \partial z^2} + \frac{\partial^2}{\partial x^2} - 2\beta\frac{\partial^2}{\partial x \partial z} + \frac{\partial^2}{\partial z^2}\right)\psi = 0. \tag{9}$$

The associated dispersion relation is discussed in the appendix. Since the nondimensional scale of the mountain is $\Delta x \sim \mathrm{Ro}^{-1}$, the differential operator in (9) is dominated at large Ro by the first two terms. Solutions in that case are hydrostatic gravity waves. When Ro is small, that is, in the quasigeostrophic limit, a balance requires $\Delta z \sim \mathrm{Ro}^{-1}$, so that the last three terms dominate. These form an elliptic operator if $|\beta| < 1$ ($N^2 > 0$ is implicit in the scaling). The corresponding disturbance is confined to the vicinity of the forcing. For intermediate values of Ro, solutions can be described as hydrostatic gravity–inertia waves modified by ''symmetric'' baroclinicity.

Steady-state linear solutions for ''bell shaped'' terrain,

$$h(x) = (1 + L^{-2}x^2)^{-1}, \tag{10}$$

are shown in Fig. 2 for $L \equiv \mathrm{Ro}^{-1} = 0.5$ and different values of β. The perturbation streamfunction, ψ (Fig. 2a), is obtained by numerically evaluating the Fourier integral shown in the appendix. Recall that the cross-ridge wind perturbation is $u = -\partial\psi/\partial z$. The long-ridge perturbation, v (Fig. 2b), comes from spatially integrating the streamfunction and using the steady-state form of (5):

$$(v + \beta\psi)_x = \psi_z.$$

Notice that the cold-advection disturbance is narrowly focused above the mountain, while the warm-advection disturbance is more scattered.

Stationary waves generally tilt upstream with height. In the case of cold advection, the same is true of the basic-state surfaces of constant ''absolute momentum,'' $\overline{M}^* \equiv fx^* + \Lambda z^*$. The relationship is illustrated schematically in Fig. 3a, where the slope of the M surfaces is shown by the steeper of the two heavy lines. As a result, v (perturbation M) is reduced in cold advection and the waves show less sensitivity to the background rotation. In warm advection, v is amplified by the larger angle between phase surfaces and M surfaces (Fig. 3b). This makes the waves more sensitive to rotation and accounts for the extra downstream dispersion evident in Fig. 2. The amplitude of the potential temperature perturbation b (not shown) has a similar sensitivity to β, as the basic isentropic surfaces tilt the same way as the absolute momentum surfaces, shown by the shallower heavy lines in Fig. 3. This has an impact on vertical dispersion in the inertial modes, a fact that will be more relevant in the case of interior forcing. The differences in the wave fields can also be explained directly from the dispersion relation and group velocity based on (9). The details are covered in the appendix.

For the present investigation we are primarily interested in upstream effects. As noted in the appendix, there are no scales at which energy can propagate upstream in stationary waves except in cold advection. In cold advection, there is a slight upstream component of the group velocity in the range $k^2 > (1 - \beta^2)/\beta^2$, where k is the horizontal wavenumber, but very little of this energy appears at low levels. At low levels, most of the steady, upstream disturbance is due to the ''trapped'' response, associated with small k and large horizontal scales. The response to the terrain (10) with $L \gg 1$, can be written in closed form as

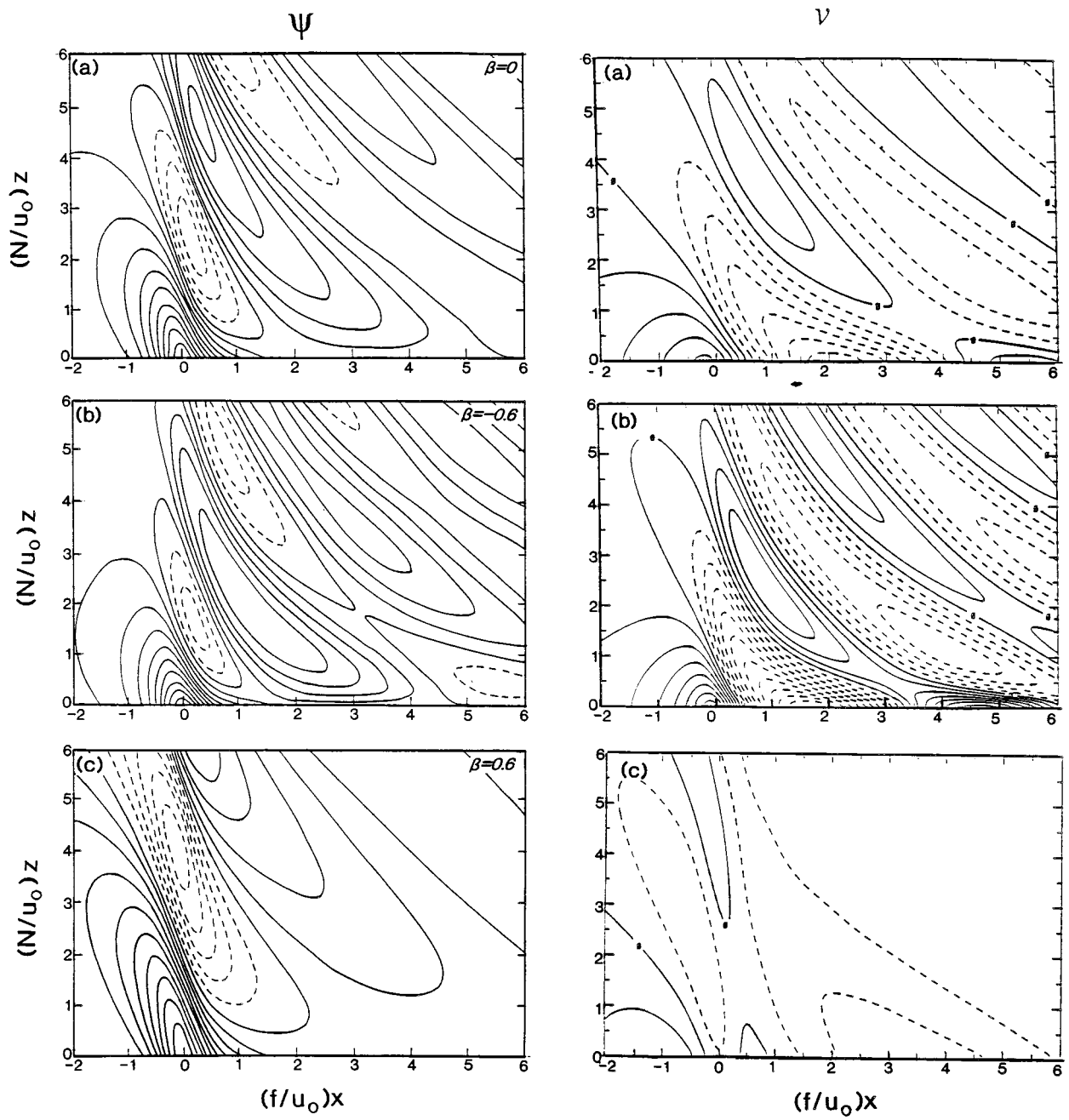

FIG. 2. Steady, linear solutions for flow over a bell-shaped mountain with halfwidth $\mathrm{Ro}^{-1} = 0.5$ and (a) $\beta = 0$, (b) $\beta = -0.6$, and (c) $\beta = 0.6$. Perturbation streamfunction ψ is shown on the left and perturbation long-ridge velocity v on the right. Horizontal and vertical distances are scaled by u_0/f and u_0/N, respectively. Contour intervals: $\delta\psi = 0.1u_0h_0$ and $\delta v = 0.1Nh_0$.

$$\psi = \frac{L(Z + L)}{X^2 + (Z + L)^2}, \tag{11}$$

where $X \equiv x + \beta z$ and $Z \equiv rz$, with $r \equiv \sqrt{1 - \beta^2}$. This is the quasigeostrophic (QG) solution. Since X is proportional to $\overline{M}$, the circulation tilts downstream with height in the case of warm advection and upstream in the case of cold advection.

An important physical consequence of the coordinate transformation can be seen by expressing the velocity perturbation as

$$u = rU - \beta W,$$
$$w = W, \tag{12}$$

where the uppercase variables represent the velocity of the barotropic solution, that is, $(U, W) \equiv (-\psi_Z, \psi_X)$. Since U and W tend to be out of phase over broad terrain,

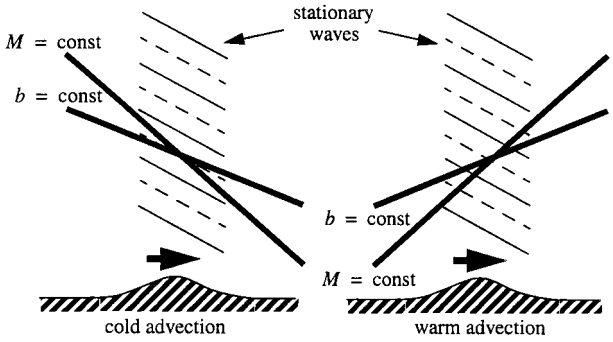

FIG. 3. Schematic diagram contrasting the relationship of stationary hydrostatic waves to environmental surfaces of potential buoyancy and absolute momentum in the case of (left) cold advection and (right) warm advection.

the u anomaly is shifted by a distance of order βL in the streamwise direction. In the case of warm advection, this brings accelerated flow onto the windward flank and weakens the decelerated region farther upstream, as seen in the linear solution, Fig. 1a. The result also follows from familiar QG principles and the fact that streamwise advection of $\overline{b}$ is frontolytical upstream whereas vertical advection of $\overline{v}$ tends to intensify the vertical shear in the same location.

Linear transience due to start-up was found to have a negligible amplitude immediately upstream of the mountain, compared to the steady disturbance there. Why should this be so? In the frame moving with the basic flow, the group velocity vector is always parallel to the phase lines, since

$$\frac{c_{gz}}{c_{gx} - 1} = -\frac{k}{m}. \tag{13}$$

For noticeable upstream effects, one needs k/m small and positive. But (A2) implies that $k/m = \pm\sqrt{\nu^2 - 1}$, where ν is the intrinsic frequency (β is neglected for clarity). Hence, upstream transients must have $\nu \approx -1$. Furthermore, since

$$c_{gx} = 1 - m^{-1}(1 + m^2/k^2)^{-1/2} \tag{14}$$

(neglecting β again), upstream energy propagation, or $c_{gx} < 0$, requires $m \ll 1$ and therefore $k \ll 1$. These restrictions on ν and k exclude most of the forcing in the linear initial-value problem.

3. Weakly nonlinear analysis

We first restore the nonlinearity to (4)–(6) by defining

$$F^{(u)} = -\mathrm{Fr}J(\psi, u) \tag{15}$$

$$F^{(v)} = -\mathrm{Fr}J(\psi, v) \tag{16}$$

$$F^{(b)} = -\mathrm{Fr}J(\psi, b), \tag{17}$$

where $J(\psi, u) = \psi_x u_z - \psi_z u_x$, etc. This nonlinear "forcing" may also be expressed in terms of eddy flux divergence. We will be evaluating the nonlinearity from the actual linear response to topography. However, it is revealing to consider immediately the Green's function solution of (4)–(6) for an interior point source that represents (15)–(17) collectively. Thus, we consider solutions of

$$L(\psi) = F_0\delta(x - x_f, z - z_f), \tag{18}$$

where L is the operator in (9), such that $\psi = 0$ at $z = 0$. The point (x_f, z_f) is the effective location of the source and F_0 represents a volume integral of the source. The result is then additive with both the linear topographic solution and the correction for weak boundary nonlinearity.

The mathematical details of the problem (18) are covered in the appendix. In Fig. 4 are shown Green's functions calculated directly from Fourier integrals for different values of β and z_f. In the two baroclinic cases, $\beta = \pm 0.6$, the slopes of the basic b and M surfaces are shown by dashed lines through the forcing points. As we will see later, the actual nonlinearity above $z = \pi$ is negligible. Since the Green's functions have no significant upstream component for $z_f < \pi$, we can therefore concentrate on the response near and below the forcing. The forcing used in Fig. 4 is $F_0 = -1$ because a mostly negative nonlinear source is expected over the mountain. The cross-mountain wind perturbation, $u = -\partial\psi/\partial z$, is negative (upstream) below such forcing.

For $z_f = \pi/4$ (Fig. 4a), a unit-amplitude negative source produces an anomaly of $u_s \approx -0.8$ in the case of both warm advection and no advection, and $u_s \approx -0.5$ in the case of cold advection. The mass-flux perturbation is $\psi_{\min} \approx -0.5$ in all cases. For $z_f = \pi/2$ (Fig. 4b), there is slightly more mass flux, $\psi_{\min} \approx -0.6$, but the surface wind perturbation weakens to about -0.5 and -0.4 for the cold-advection and barotropic solutions, respectively. Interestingly, the surface wind in the warm-advection solution remains at -0.8 for the higher source, as the center of the circulation is substantially lower than in the other two cases.

The effect of baroclinicity on the trapped part of the Green's function can be understood by using the skewed coordinate system introduced in (11). The velocity components are

$$u = U - \beta W/r,$$

$$w = W/r, \tag{19}$$

where the uppercase variables represent the barotropic solution. At the ground, we impose $W = 0$. Hence, the quasigeostrophic contribution to the horizontal wind perturbation is greatest where U is greatest, at $x = x_f + \beta z_f$. This point is on the same basic M surface that contains the source. Hence, an upstream response to the forcing is favored when $\beta < 0$.

The baroclinic effect on the propagating part of the response can be understood largely from the properties of the group velocity discussed in the appendix. For the

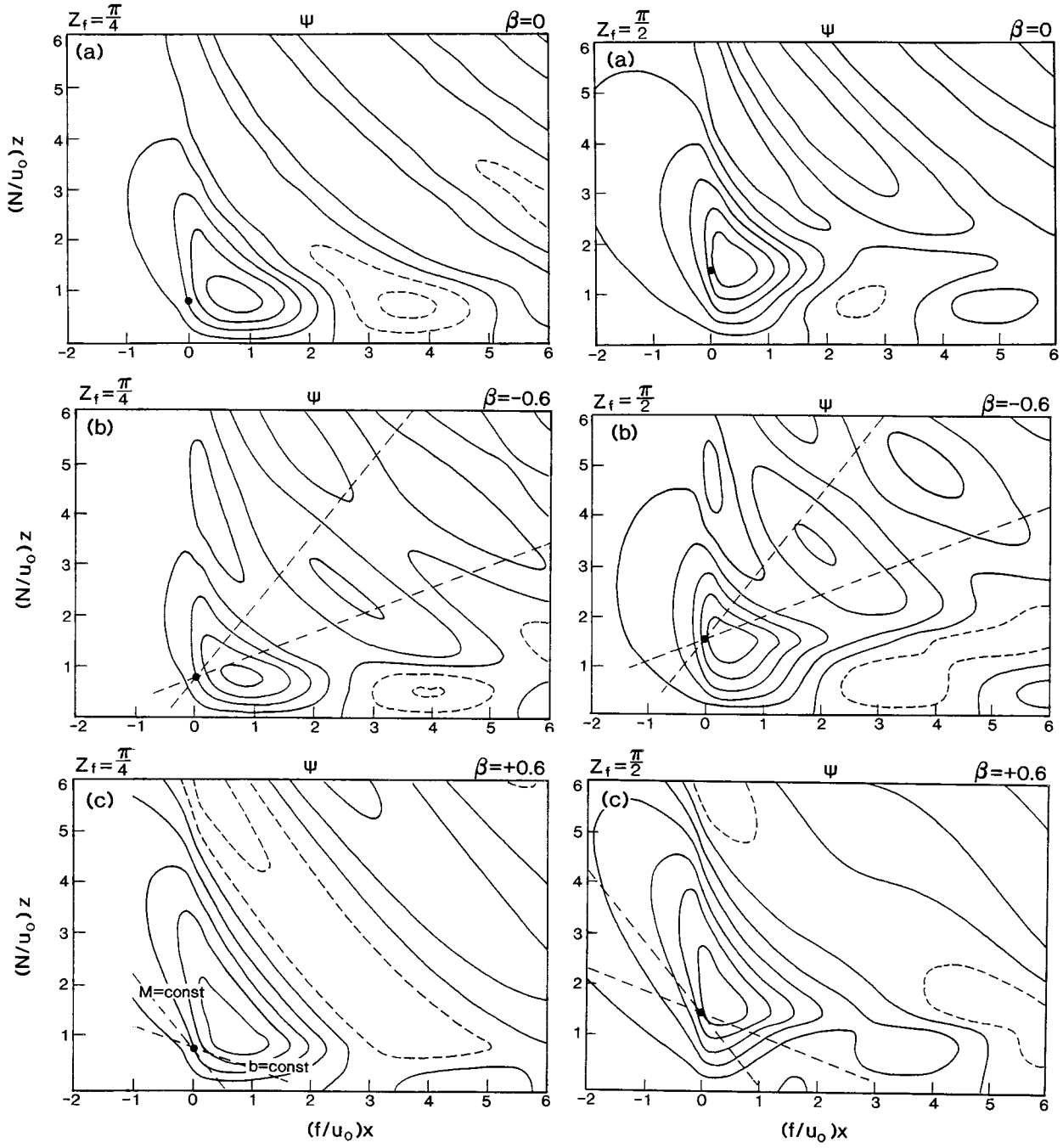

FIG. 4. Steady, linear response to negative line sources located at points indicated by dots. Baroclinicity is (a) $\beta = 0$, (b) $\beta = -0.6$, and (c) $\beta = 0.6$. Results on the left are for a forcing height $z_f = \pi/4$ and those on the right are for $z_f = \pi/2$. Dashed lines drawn through forcing points indicate slopes of basic absolute momentum surfaces (steeper line) and isentropes. Contour interval: $\delta\psi = 0.1u_0h_0$. Axes as in Fig. 2.

same reason that cold advection focuses wave energy above the mountain in the linear response to topography, warm advection creates a broader range of downward-propagating modes with negligible streamwise propagation. This focuses and amplifies the disturbance below the source. As noted in the appendix, the downward propagating modes grow in relative importance as $\beta \rightarrow -1$ or $z_f \rightarrow \infty$. Their effect compensates for the decreasing contribution from the modes with $k \gg 1$ as the forcing is raised.

If $\beta > 0$, rotational effects are suppressed and energy is concentrated above the source, as clearly seen in Fig. 4. A similar concentration above the forcing in the topographic solution is probably responsible for the wave

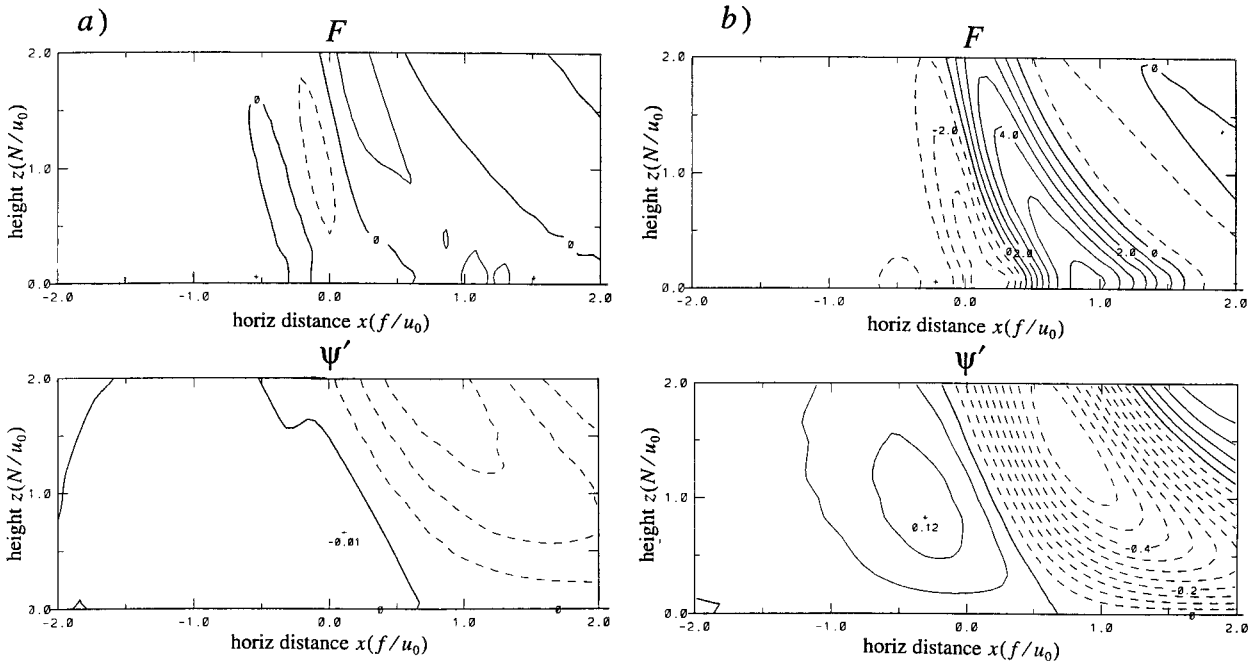

FIG. 5. Nonlinear source distribution and streamfunction response for (a) $\beta = 0$ and (b) $\beta = -0.6$. Contour intervals: $\delta F = 1.0\,\mathrm{Fr}$ and $\delta\psi = 0.05\,\mathrm{Fr}$, where F and ψ are normalized as indicated in text. Axes as in Fig. 2.

drag enhancement seen in Fig. 8 of Part I. In warm advection, the linear mountain drag is enhanced directly by the amplification of the buoyancy anomaly.

The distribution of the nonlinearity will be obtained from small-Fr simulations using (15)–(17). From (4)–(6), the problem for the $O(\mathrm{Fr})$ streamfunction correction, which we call ψ_1, is

$$L(\psi_1) = F_{0x}^{(b)} - F_{0z}^{(v)} - F_{0xz}^{(u)}, \tag{20}$$

where $F_0^{(b)}$, $F_0^{(v)}$, and $F_0^{(u)}$ are evaluated from the linear solution. For example,

$$F_0^{(b)} = -\mathrm{Fr}J(\psi_0, b_0). \tag{21}$$

The first two forcing terms in (20) represent the tendency of the stationary eddy fluxes to produce thermal wind imbalance. The third may be ascribed to eddy vorticity flux, since

$$-F_z^{(u)} = -F^{(\omega)} = \mathrm{Fr}J(\psi, \omega), \tag{22}$$

with $\omega \equiv \partial u/\partial z$, the horizontal vorticity.

Certain properties of the nonlinearity can be anticipated. The Eliassen–Palm theorem implies that the horizontal integral of $F_0^{(u)}$ vanishes in the nonrotating limit. Long (1953) and Smith (1977) showed that $F_0^{(\omega)}$ and $F_0^{(b)}$ are identically zero in that limit. Of course, $F_0^{(v)}$ is also zero in the absence of rotation. Hence, all weakly nonlinear corrections of the steady solution are due, either directly or indirectly, to background rotation. On the other hand, rapid rotation ($\mathrm{Ro} \to 0$) effectively removes the nonlinearity, since u and w are $O(\mathrm{Ro})$ smaller than v in quasigeostrophic solutions.

It was supposed in G86 that the first forcing term, $\partial F_0^{(b)}/\partial x$, in (20) would dominate in the strongly baroclinic cases. The argument given there was that $F_0^{(b)}$ incorporates the effect of altered vertical stratification due to a tilting of the ambient horizontal stratification by the lowest-order circulation. The vertical stratification tends to be reinforced over the windward slope in this way if $\beta < 0$. The buoyancy forcing does dominate in the quasigeostrophic limit (with a different physical interpretation) because vorticity advection is generally negligible in that regime. However, the situation is different at order-unity Ro. While $F_0^{(b)}$ is maximized in the right place and with the right sign in warm advection in that case, we will see that it is dominated by $F_0^{(\omega)}$. McIntyre (1972) states a similar conclusion for the transient nonlinear ''forcing'' in the nonrotating problem.

The distribution of total steady-state sources in the form $F = -F_{0x}^{(\omega)} + F_{0x}^{(b)} - F_{0z}^{(v)}$ and the streamfunction response, ψ_1, for the bell-shaped mountain (10) with $L = 0.5$ are shown in Fig. 5a for $\beta = 0$ and Fig. 5b for $\beta = -0.6$. The sources are obtained as a function of time by running the numerical model from initial values with extremely small Fr. The weakly nonlinear response is then obtained by running the model again to steady-state with the time-dependent forcing inserted into the prognostic equations. In the second run, there is no terrain (so the nonlinear sources are not duplicated). The reason for using time-dependent sources is to be able to assess the representativeness of the steady response in the context of the initial-value problem.

The steady-state results in Fig. 5 are renormalized as

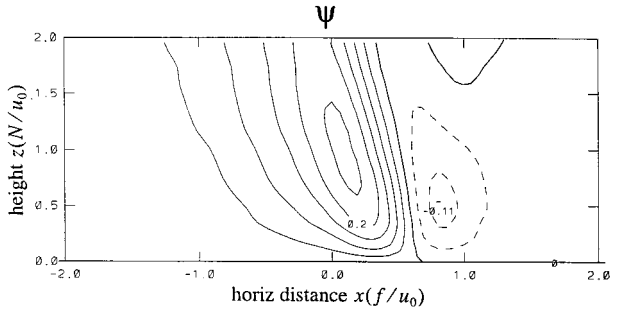

FIG. 6. Source due to (a) vorticity advection (F_A) and (b) combined temperature advection and long-ridge velocity advection (F_B) for Ro = 2.0 and $\beta = -0.6$. Contour intervals and axes as in Fig. 2.

though Fr = 1. In the warm-advection case (Fig. 5b), the response has $u_s = -0.32$ at the point of maximum surface deceleration. The barotropic result is almost an order of magnitude weaker, and the cold-advection result (not shown) is weaker still. The near-field pattern is established during an order-unity elapsed time following start-up. This is consistent with the principle that the wave front separating disturbed and undisturbed flow moves upward at roughly the vertical group speed of the stationary waves, $c_{gz} = |k|/m^2 \sim$ Ro. The analysis in the appendix shows that the transience becomes less important in generating nonlinearities than the steady waves after an elapsed time of O(R1). In the time-dependent model calclulation leading to Fig. 5b, the near-field source strength peaks at $t \approx 1.5$ with about 150% of the steady-state amplitude. The transient streamfunction response at $t = 1.0$ is shown in Fig. 6 for the case of warm advection. The result for $\beta = 0$ (not shown) is quite similar upstream of $x = 0.5$. Notice that the strongest initial deceleration is displaced to the lee of the mountain. There is no evidence of this effect in the fully nonlinear initial-value solutions (cf. Figs. 4a and 5a of Part I). Thus, the start-up is poorly represented by the steady-state weakly nonlinear expansion when Fr = O(1).

In Fig. 7, the stationary nonlinearity in the warm-advection case is separated into the two contributions, $F_A + F_B = F$, where

$$F_A \equiv -F_{0x}^{(\omega)}, \tag{23}$$

$$F_B \equiv F_{0x}^{(b)} - F_{0z}^{(v)}. \tag{24}$$

The nonlinearity due to vorticity advection, F_A, clearly dominates. In computing F_B, we found that the forcing due to $F_0^{(v)}$ (not shown) largely offsets the expected negative values near the mountain due to buoyancy advection. However, each of the terms is already much smaller than F_A.

To see why F_A must be at least comparable to the other nonlinearity, we first express all of the sources in terms of the meridional displacement, η. Consider the steady-state forms of (4)–(10). Differentiating (4) with respect to z, substituting from (7), and integrating in x

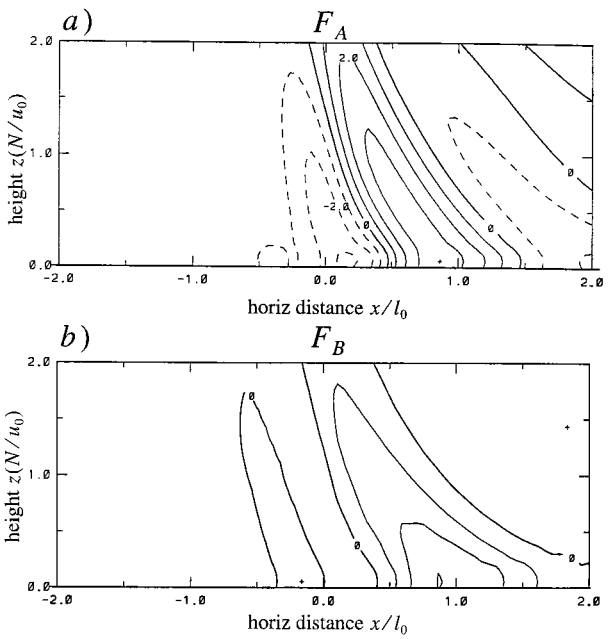

FIG. 7. Streamfunction response to full nonlinear forcing in warm advection ($\beta = -0.6$) at $t = 1.5$ during start-up. Countours and axes as in Fig. 5.

yields $\omega_0 = -b_0 + \eta_{0z}$. Here η is in units of Nh_0/f and satisfies

$$\eta_x = v. \tag{25}$$

From the steady-state versions of (5) and (6), we also have that $b_0 = \beta v_0 - r^2\psi_0$. Hence, $\omega_0 = -\beta\eta_{0x} + \eta_{0z} + r^2\psi_0$. The term proportional to ψ_0, due to vertical displacements, will have no effect in (20). Therefore, the source due to vorticity advection is

$$F_A = \mathrm{Fr}\frac{\partial}{\partial X}J(\psi_0, \eta_{0Z}). \tag{26}$$

Here we have changed to the absolute-momentum coordinates, $X = x + \beta z$ and $Z = z$. Using the same coordinate system, the other sources may be written as

$$F_B = \mathrm{Fr}\frac{\partial}{\partial Z}J(\psi_0, \eta_{0X}). \tag{27}$$

From (26) and (27), there is no obvious way to choose between F_A and F_B as the dominant nonlinearity.

Let λ_x and λ_z represent nondimensional horizontal and vertical scales. Then since $\psi_0 = O(1)$ and [in view of (25) and (5)] $\eta_0 = O(\lambda_x^2/\lambda_z)$, both (26) and (27) can be estimated as $F \sim \mathrm{Fr}/\lambda_z^3$. The streamfunction correction, ψ_1, is of the order of the volume integral of the source, or $\langle F\rangle \sim \mathrm{Fr}\lambda_x/\lambda_z^2$. The mountain scale is $\lambda_x = \mathrm{Ro}^{-1}$. If this is small, then $\lambda_z = O(1)$ and

$$\psi_1 \sim \mathrm{FrRo}^{-1}, \tag{28}$$

which shows the expected vanishing of the forcing in

the nonrotating limit. If the mountain is broad, then the dominant scales have $\lambda_z \approx \lambda_x$ and

$$\psi_1 \sim \mathrm{FrRo}. \tag{29}$$

These estimates are upper bounds; the nonlinearity also depends on the phase relationships between $\psi(X, Z)$ and $\eta(X, Z)$. Indeed, (28) overestimates ψ_1 by a factor of 5 in the warm-advection case with Ro = 2 (Fig. 5b) and by more than an order of magnitude in the barotropic solution. The steady-state form of (9) implies

$$v_{0X} = \psi_{0Z}. \tag{30}$$

This means that v (and therefore η_X and η_Z) tends to be in phase with ψ for the small horizontal scales. Because of the Jacobians in (26) and (27), this gives the large-scale components a disproportionate importance near the mountain. For such scales, (29) overestimates the forcing due to vorticity advection because $\omega = O(\mathrm{Ro})$ compared to gradients of v and b. This degeneracy manifests itself as $\eta_{0Z} \to 0$ in (26) but does not affect (27).[1]

From (26) and (27), we see that the sensitivity of the nonlinearity to ambient baroclinicity is partly due to the effect of β on the meridional displacement η. This displacement increases, along with v, in warm advection. The angle between the M surfaces and the phase surfaces further impacts the forcing through the constant-$\overline{M}$ derivatives in (26) and (27). In the case of (27), the first effect represents the increased thermal wind imbalance at lowest order due to the amplification of v_0 and b_0 in warm advection. The second shows the dependence of thermal wind balance on the correlation between v and b. For example, if $\beta > 0$, upstream-tilting η surfaces yield a correlation that suppresses the baroclinic production of any vorticity that can be advected by ψ_0. The fact that $F_B \ll F_A$ (Fig. 7) stems from a particularly unfavorable phase relationship between η_{0x} and ψ_0. The physical interpretation of this is probably quite subtle.

Analysis of the Green's function in the appendix shows that the response to forcing is greatest when the forcing height is about unity. In Fig. 5, the area integral of the significant forcing over the mountain, say between $z = 0.5$ and $z = 1.5$ and between $x = -0.2$ and $x = 0.2$, may be estimated as $\langle F \rangle \approx -0.4\,\mathrm{Fr}$. Since the Green's function for Ro = 2 and $\beta = -0.6$ has a maximum surface response of $u_s = -0.8$, this is consistent with the result $u_1 = -0.3\,\mathrm{Fr}$ for the barrier enhancement implied by Fig. 5b.

At lowest order, the maximal surface deceleration is $u_{sm} \approx -0.4$ near $x = -1.0\,\mathrm{Ro}^{-1}$ (Fig. 1a). If we assume, for the moment, that the maximum nonlinear correction of $-0.3\,\mathrm{Fr}$ extends upstream to this point, then the surface deceleration for the Ro = 2 bell-shaped mountain is

$$u_{sm} = -0.4\,\mathrm{Fr} - 0.3\,\mathrm{Fr}^2 + O(\mathrm{Fr}^3), \tag{31}$$

where u_{sm} is now in units of u_0. The terms up to $O(\mathrm{Fr}^2)$ closely approximate the result for warm advection in Fig. 1b. Thus, setting $1 + u_{sm} = 0$ and neglecting $O(\mathrm{Fr}^3)$ effects leads to the estimate Fr = 1.3 for the stagnation threshold. This is quite close to the actual threshold indicated in Fig. 3 of Part I for Ro = 2 and $\beta = -0.6$. For $\beta = -0.9$ and the same Ro (not shown), the weakly nonlinear analysis yields $u_1 \approx -0.5\,\mathrm{Fr}$. Since the linear response is relatively insensitive to β, we can write

$$u_{sm} = -0.4\,\mathrm{Fr} - 0.5\,\mathrm{Fr}^2 + O(\mathrm{Fr}^3) \tag{32}$$

for Ro = 2 and $\beta = -0.9$. Stagnation is therefore predicted at Fr = 1.1. The actual threshold in this case is $\mathrm{Fr}_s = 1.0$. In cold advection, it is fair to take $u_1 \approx 0$ for the nonlinear correction, so that

$$u_{sm} \approx -0.4\,\mathrm{Fr} + O(\mathrm{Fr}^3). \tag{33}$$

This leads to $\mathrm{Fr}_s \approx 2.5$ for $\beta > 0$, which is a fairly good description of the cold-advection results in Fig. 3 of Part I.

The quantitative success of the (31)–(33) at order-unity Fr is somewhat fortuitous, since the surface flow deceleration due to weak nonlinearity does not really coincide with that of the linear solution. The assumption of coincident surface perturbations compensates for an underestimate of the overall strength of the upstream correction. These circumstances can be seen in Fig. 8, which shows the x dependence of the steady-state surface wind perturbations for the linear, fully nonlinear, and weakly nonlinear (two-term expansion) solutions. The model parameters are Fr = 1.2, Ro = 2, and $\beta = -0.6$, just below the stagnation threshold. While the expansion misses the amplitude of the minimum u_s by only about 10%, its failure to capture the upstream displacement of the deceleration is significant. Recall that the latter error was even worse for the transient solution (Fig. 7). There is no significant improvement when the first nonlinear correction is recalculated from a nonlinear model run in which the sources are scaled back up to Fr = 1.2, as shown in Fig. 8. This means that the nonlinear source is not sufficiently isolated from the response to allow the method to be used with high accuracy at order-unity Fr.

4. Summary and conclusions

Part I established that large-scale warm advection, $\beta < 0$, favors stagnation by lowering the Fr threshold while cold advection inhibits it. It also established a maximum mountain width (inverse Ro) for stagnation, and, in the case of strong warm advection ($\beta < -0.5$), a minimum width as well. The upper bound on the width limits the influence of background rotation. The lower bound (in the case of strong warm advection) keeps the

[1] The expansion in powers of Fr is unnecessary in the quasigeostrophic limit if $\beta = 0$. In that case, the nonlinearity can be treated exactly using a coordinate transformation (Pierrehumbert 1985). The transformation thus isolates the nonlinearity due to $\beta \neq 0$ (G86), but adds little to the present discussion using (19).

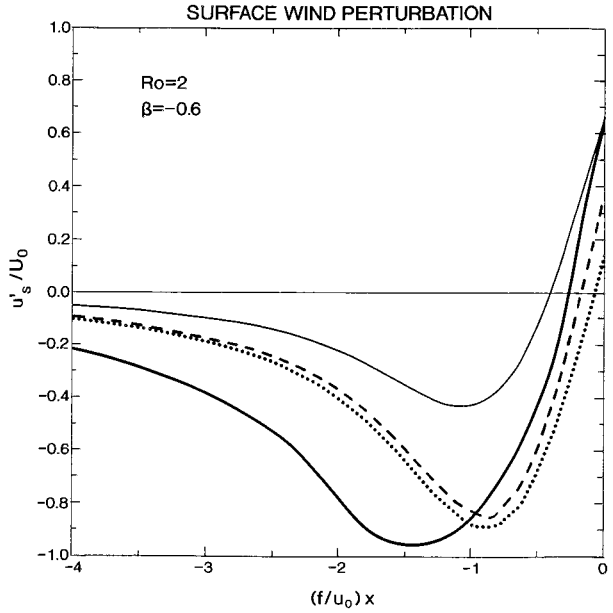

FIG. 8. Steady, cross-mountain surface wind perturbation in warm advection ($\beta = -0.6$) at Fr = 1.2 as a function of horizontal distance. Mountain ridge is centered at $x = 0$. Various curves represent linear (thin solid), nonlinear (thick solid), and weakly nonlinear (dashed or dotted) model calculations. Weakly nonlinear calculations are based on two terms in the Fr expansion, with dotted curve showing the result of using fully nonlinear response to lowest-order nonlinearity. The linear result is scaled up to Fr = 1.2 to show first term in expansion. Horizontal axis scaled by u_0/f.

terrain broad enough for the ambient isentropic slope to be significant on the scale of the mountain circulation.

The linear response to isolated topography shows just the opposite sensitivity to baroclinicity: warm advection weakens the barrier effect, while cold advection strengthens it. At small amplitude, the upstream disturbance is dominated by large scales because the group velocity in the small scales is directed downstream. Therefore, the linear result in each case can be understood as mainly a quasigeostrophic response to streamwise advection of $\overline{b}$ and vertical advection of $\overline{v}$.

The quasigeostrophic contribution to the weakly nonlinear correction is consistent with enhanced upstream deceleration in warm advection. However, for mesoscale terrain, Ro $\geq O(1)$, the weakly nonlinear analysis shows that the correction is dominated by the nonlinearity in the ageostrophic, cross-mountain momentum equation. This overwhelms not only the the QG effect but also the nonlinearity due to nongeostrophic scales in the temperature equation. The large-scale warm advection in the mesoscale regime amplifies the thermal wind imbalance and horizontal vorticity production because of the mismatch between the gravity wave particle displacements and the ambient buoyancy and momentum contours. When the low-level streamwise advection is slowed down, in effect, by the weakly nonlinear correction, the enhanced vorticity production results in additional low-level negative momentum perturbation upstream.

The weakly nonlinear analysis assumes that the upstream surface wind can be expanded as

$$u_s = 1 + a_1(\mathrm{Ro}, \beta)\mathrm{Fr} + a_2(\mathrm{Ro}, \beta)\mathrm{Fr}^2 + O(\mathrm{Fr}^3), \quad (34)$$

where u_s is normalized by u_0. Linear solutions show that a_1 varies by only about 0.05 as a function of β at Ro = 2, whereas a_2 was found to vary by about 0.5 (mostly in the warm-advection range of β). Hence, the small-amplitude effect of β is dominated by the finite-amplitude effect if Fr $\gg 0.1$. This is a weaker condition on Fr than the condition for nonlinearity. The results in Fig. 8 and (31)–(33) show that the weakly nonlinear calculation can explain much of the baroclinic effect near the stagnation threshold without transient effects or higher-order nonlinear effects. The approach works better upstream because the linear dispersion properties filter out small horizontal scales there, partially isolating the nonlinearity from the response. The approach is expected to be less successful in the downstream region, although the downstream low-level acceleration (Fig. 5) is qualitatively correct.

Wave breaking occurs at smaller amplitude in warm advection than in cold advection mainly because the ambient isentropic surfaces are tilted against the particle displacements in stationary waves (the same reason that vorticity production is enhanced). In cold advection, the isentropes are more oblique to the particle displacements. The symmetry of the drag dependence on β in Fig. 8 of Part I seems to be accidental, as the physical reasons for the increase suggested here are different for warm and cold advection. The high sensitivity of the total drag to Fr in warm advection and low sensitivity in cold advection may be related to the similarly skewed β dependence of a_2 in (34). However, we have not applied the weakly nonlinear analysis specifically to the drag. The unexpectedly smooth transition in drag across the wave breaking threshold in warm advection may simply mean that the sensitivity to Fr is strong enough to mask the effect of a sharply altered downstream flow due to wave breaking. This is a matter for further study.

Acknowledgments. I am grateful to Yoshio Kurihara, Isidoro Orlanski, Kerry Emanuel, and the reviewers for suggestions that improved the manuscript. The figures were prepared by Catherine Raphael.

APPENDIX

Linear Response to Topography and Interior Sources

From (8)–(12), linear disturbances are governed by

$$\left[\left(\frac{\partial}{\partial t} + \frac{\partial}{\partial x}\right)^2 \frac{\partial^2}{\partial z^2} + \frac{\partial^2}{\partial x^2} - 2\beta\frac{\partial^2}{\partial x \partial z} + \frac{\partial^2}{\partial z^2}\right]\psi = 0. \quad (A1)$$

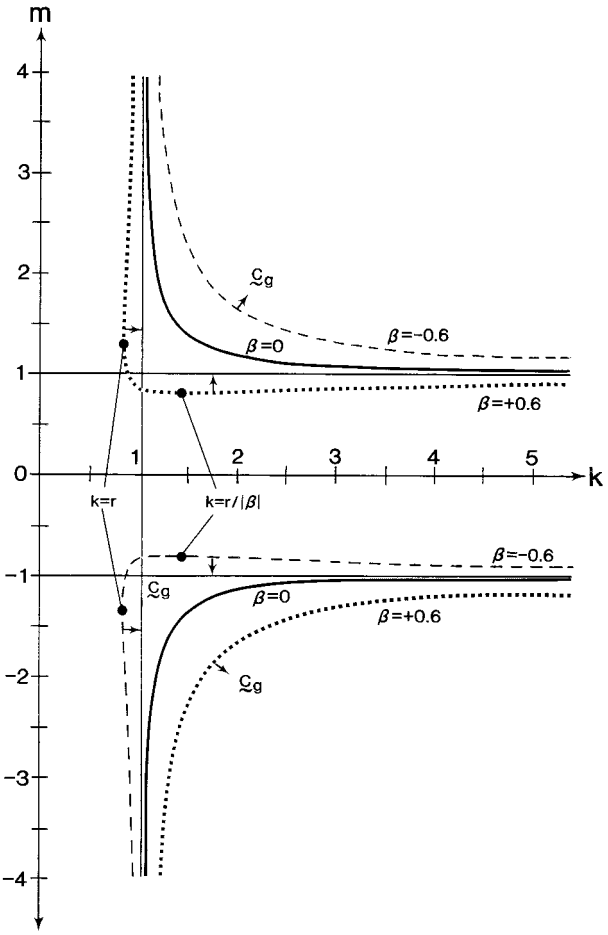

FIG. A1. Graph of dispersion relation between horizontal and vertical wavenumbers, k and m, for stationary waves in barotropic ($\beta = 0$) and baroclinic ($\beta = \pm 0.6$) basic states. Arrows indicate the direction of group velocity if the axis coordinates are regarded as physical distance.

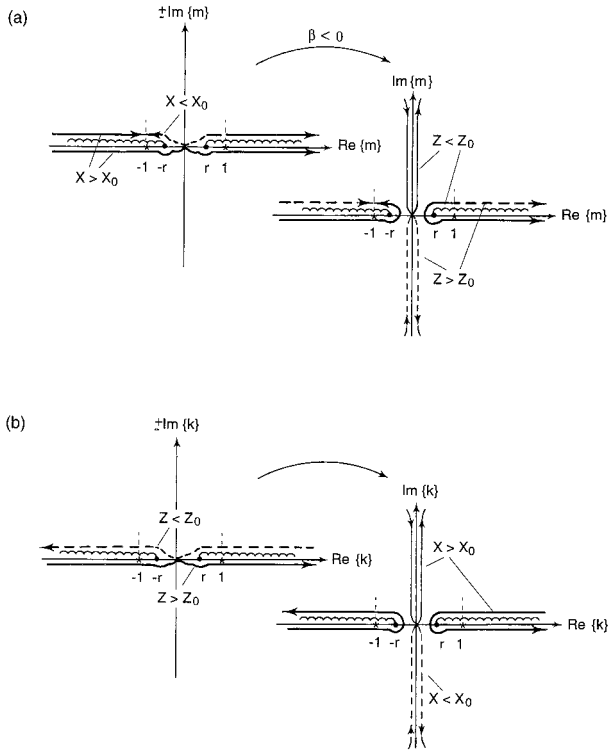

FIG. A2. Original and deformed complex Fourier integration paths for (a) vertical and (b) horizontal transforms. Branch points appear at k or $m = \pm r$, and essential singularities at k or $m = \pm 1$. In left-hand diagrams, imaginary axis is multiplied by the sign of $z - z_0$ or $x - x_0$ in order to avoid redrawing the branch cuts. The direction of integration is indicated by arrows.

For normal modes of the form $\psi = \tilde{\psi} \exp[i(kx + mz - \nu t)]$, we therefore have

$$(k - \nu)^2 m^2 - k^2 + 2\beta km - m^2 = 0. \qquad \text{(A2)}$$

The time-dependent problem will be considered below in a simplified form. For steady modes,

$$k^2 - 2\beta km + m^2 - k^2 m^2 = 0. \qquad \text{(A3)}$$

Hence, for a given k, there are two solutions for m, corresponding to the two branches of the square root in

$$m(k) = \frac{\beta k}{1 - k^2} + \frac{k(k^2 - r^2)^{1/2}}{k^2 - 1}, \qquad \text{(A4)}$$

where $r \equiv \sqrt{1 - \beta^2}$. Real values of $m(k)$ are graphed in Fig. A1 for $\beta = 0$ and $\beta = \pm 0.6$.

The slope of the group velocity vector (c_{gx}, c_{gz}) is

$$\frac{c_{gz}}{c_{gx}} = \frac{\partial \nu / \partial m}{\partial \nu / \partial k} = -\left(\frac{dk}{dm}\right)_{\nu = \text{const}}. \qquad \text{(A5)}$$

Therefore, if the coordinates in Fig. A1 are regarded as horizontal and vertical distance, energy propagation in a component (k, m) is in the direction perpendicular to the graph and away from the coordinate axes. For lower-boundary topography, the branch with $c_{gz} < 0$ is irrelevant. For interior forcing above a lower boundary, both branches are relevant below the forcing level.

As $k \to \infty$, buoyancy oscillations become free of ''inertial'' effects and the vertical wavenumber asymptotes to $m = 1$. Inertial oscillations become free of buoyancy effects as $m \to \infty$, which corresponds to the asymptote $k = 1$. The group velocity is exactly vertical in the first limit and exactly horizontal in the second. If $\beta \neq 0$, such ''pure'' oscillations are also possible for certain finite scales. Examining intrinsic frequencies reveals that one of the $k = r$ solutions is a pure buoyancy oscillation and one of the $m = \pm r$ solutions acts as a pure inertial mode. It can be shown that the respective particle displacements are exactly parallel to the basic ''absolute momentum'' surfaces (constant $fx + \overline{v} \equiv \overline{M}$) and basic isentropes. This eliminates either the buoyancy perturbation or the meridional velocity perturbation. In cold advection, the tilt of the basic M surfaces is of the same sign as the phase surfaces in an upward-

propagating gravity wave train (cf. Fig. 3a). This suppresses inertial effects and maintains $m \approx 1$ over a broad range of horizontal scales, thereby focusing energy above the forcing. At the same time, the lower branch becomes more dispersive and energy is scattered more broadly over the region below and downstream of the forcing. If $\beta < 0$, the two branches are interchanged, so that the upward-propagating signal becomes more dispersive and the downward-propagating signal more concentrated.

For the special mountain profile $h = \delta(x)$, the perturbation streamfunction is

$$\psi(x, z) = \frac{1}{2\pi} \int_{-\infty}^{\infty} \exp\{i[kx + m(k)z]\}\, dk, \quad \text{(A6)}$$

which satisfies $\psi(x, 0) = h(x)$. To satisfy a radiation condition at $z \to \infty$, we choose the upper branch in (A4), that is, $(k^2 - r^2)^{1/2} > 0$, in the intervals $k^2 > r^2$. For all other real k, we choose $\mathrm{Im}\{(k^2 - r^2)^{1/2}\} < 0$ for boundedness at $z \to \infty$. This converts (A6) to two integrals with real-valued integrands, namely

$$\psi = \frac{1}{\pi} \int_0^r \exp(-\tilde{m}_1 z) \cos\left[k\left(x + \frac{\beta z}{1 - k^2}\right)\right] dk + \frac{1}{\pi} \int_r^{\infty} \cos\left[k\left(x + \frac{\beta z}{1 - k^2}\right) + m_1 z\right] dk, \quad \text{(A7)}$$

where $m_1 = k\sqrt{k^2 - r^2}/(k^2 - 1)$ and $\tilde{m}_1 = k\sqrt{r^2 - k^2}/(1 - k^2)$. The quasigeostrophic part of the solution is easily seen by letting $k \to 0$ in the first integral and ignoring the finite upper limit of integration. Thus,

$$\psi_{qg} = \frac{1}{\pi} \int_0^{\infty} \exp(-rkz) \cos[k(x + \beta z)]\, dk, \quad \text{(A8)}$$

which may be evaluated, using the coordinates defined for (11), as

$$\psi_{qg} = (1/\pi) \frac{Z}{X^2 + Z^2}. \quad \text{(A9)}$$

This is valid in $X^2 + Z^2 \gg 1$. The second integral in (A7) provides the near-field solution but diverges at $x = 0$ due to large k. Hence, the solutions displayed in section 3 are for a regular mountain with halfwidth L and Fourier transform $\hat{h}(k) = (L/2) \exp(-|k|L)$.

Now if the point source $\delta(x - x_0, z - z_0)$ is substituted for the right-hand side of (A1), (A4) may be used to write the linear response to interior forcing as

$$\psi = -\frac{1}{2\pi} \int_{-\infty}^{\infty} \exp\left[ik\left(x - x_0 + \frac{\beta(z - z_0)}{1 - k^2}\right)\right] \times \frac{\exp(im_1|z - z_0|) - \exp(im_1(z + z_0))}{2ik\sqrt{k^2 - r^2}}\, dk, \quad \text{(A10)}$$

where $m_1(k)$ is defined as in (A7). The term involving $z + z_0$ enforces the boundary condition, $\psi = 0$ at $z = 0$, and can be interpreted as a reflection of the downward-propagating components. The absolute-value operator implicitly selects the lower branch of $m(k)$ for unreflected waves below the source.

Certain asymptotic approximations are possible for (A10). The standard far-field approximation is a combination of the QG solution and the stationary-phase approximation. The QG solution was discussed in section 3. The stationary-phase estimate, which is analogous to tracing group-velocity ''rays'' into regions far from the forcing, is treated in G86. Here we will be interested in the near-field approximations, especially below the forcing level.

a. Near-field approximations of the Green's function

The horizontal near-field approximation of (A10), valid in $|x - x_0| \ll 1$, is obtained by assuming $k \gg 1$ and therefore $m \to 1$. The result

$$\psi_G = -\frac{1}{2\pi} \int_{k_1}^{\infty} \frac{\sin(k(x - x_0) + |z - z_0|) - \sin(k(x - x_0) + z + z_0)}{k^2}\, dk + C_G \quad \text{(A11)}$$

is the contribution from the barotropic gravity waves. The missing wavenumbers $k < k_1$ determine C_G, which, for consistency, must be considered independent of x in this approximation. The constraint $k_1 \gg 1$ determines the region of validity of the x-dependent part of ψ_G, which shrinks with increasing vertical distance from the source. The estimate (A11) may be evaluated as

$$\psi_G = -\sin z_0 \left(\frac{|x - x_0|}{2} \cos z - \frac{(x - x_0)}{\pi} \log|x - x_0| \sin z\right) + C_G(z) \quad \text{(A12)}$$

in $z > z_0$. Below the forcing, z and z_0 must be interchanged.

The way to obtain the integration constant C_G is suggested by a procedure used by Queney (1947) and Pierrehumbert (1984) to find the velocity perturbation along a topographic boundary. The Green's function is first rewritten as a vertical transform (G86) and reduced to one dimension by setting $x = x_0$. Thus,

$$\psi(x_0, z) = \frac{1}{2\pi}\int_{-\infty}^{\infty} \frac{\exp[im(z - z_0)]}{2im\sqrt{m^2 - r^2}}\, dm + (\text{reflections}). \tag{A13}$$

The integral for the reflected modes is not shown because it is unwieldy when $\beta \neq 0$. Reflections are obviously significant at $z = 0$, but we assume that the solution is dominated by unreflected waves at the forcing level. Next, to isolate the gravity wave contribution, the complex integration path is altered as shown in Fig. A2. In the region of physical space where $\beta(z - z_0) > 0$ (below the forcing if $\beta < 0$), the result is

$$\begin{aligned}\psi(x_0, z) = &-\frac{1}{2\pi}\int_0^{\infty} \frac{\exp(-\tilde{m}|z - z_0|)}{\tilde{m}\sqrt{\tilde{m}^2 + r^2}}\, d\tilde{m} \\ &- \frac{1}{2\pi}\left(\int_r^{\infty} \frac{\sin m|z - z_0|}{m\sqrt{m^2 - r^2}}\, dm \right. \\ &\left. + \int_r^{1} \frac{\sin m|z - z_0|}{m\sqrt{m^2 - r^2}}\, dm\right).\end{aligned} \tag{A14}$$

The path along the imaginary axis has been parameterized by $m = i\tilde{m}$. The gravity wave contribution is now contained in the two plane-wave integrals. In the region where $\beta(z - z_0) < 0$, these are replaced by a single integral over $(1, \infty)$ with the same integrand.

Inside $|z - z_0| \approx 1$, the long-wave (QG) contribution contained in the first integral in (A14) determines C_G. However, for $|z - z_0| \gg 1$, it is determined by the intermediate vertical scales in the two plane-wave integrals. These can be related to the gamma function with parameter ½ by letting $m = r + \varepsilon$ and assuming $\varepsilon \ll 1$. Thus, the integration constant in (A12) is estimated to be

$$C_G(z) \approx -\frac{1}{2r}\frac{\sin(r|z - z_0| + \pi/4) + A_1 \sin(r|z - z_0| + \phi_1)}{(2\pi r|z - z_0|)^{1/2}} \tag{A15}$$

far above and below the source. The second of the gravity wave integrals in (A14) has been approximated by the incomplete gamma function, $\Gamma(z_1; ½)$, with $z_1 = (1 - r)|z - z_0|$ for the integration limit. As this limit increases, A_1 varies from zero to unity, and ϕ_1 from zero to $\pi/4$, each with a damped oscillation about the higher limit. Therefore, if $|z - z_0| \gg 1/(1 - r)$, the two integrals are approximately the same and C_G has twice the amplitude of the barotropic estimate. In the same limit, the integral for $\beta(z - z_0) > 0$ vanishes. This baroclinic amplification above or below the forcing is consistent with the group velocity of the finite-scale (baroclinic) gravity waves, as mentioned in section 3. In $|x - x_0| \ll 1$, the phase is stationary near the branch point $m = r$. Consequently, we are not concerned that setting $x = x_0$ may have produced a spurious approximation.

The vertical near-field approximation is obtained by letting $m \to \infty$ and $k \to 1$ in the vertical transform integral (G86). The radiation condition in x eliminates any contribution from $|m| > 1$ in the half-plane $x < x_0$. In $x > x_0$, taking $m \gg 1$ produces

$$\psi_I = -\frac{1}{2\pi}\int_{m_1}^{\infty} \frac{\sin[m(z - z_0) + x - x_0] - \sin[m(z - z_0) - (x - x_0)]}{m^2}\, dm + C_I. \tag{A16}$$

Here C_I is due to the interval $(0, m_1)$ with $m_1 \gg 1$. The closed-form evaluation of (A16) is

$$\psi_I = \frac{|z - z_0|}{2}\sin(x - x_0) + C_I(x), \tag{A17}$$

which shows an inertial lee wave train with even symmetry about the forcing level. An estimate for C_I is obtained by redrawing the k-integration path as indicated in Fig. A2b to isolate the trapped components and evaluating the contribution from the branch point (G86). Since the finite-scale (baroclinic) inertial modes propagate only downstream, it is not necessary to include the baroclinic effect in this part of the analysis.

Thus, with $\beta = 0$ and $z = z_0$, the propagating modes contribute

$$\psi(x, z_0) \approx \frac{1}{\pi}\int_1^{\infty} \frac{\sin k(x - x_0)}{k\sqrt{k^2 - 1}}\, dk. \tag{A18}$$

The result of excluding terms past second order in the parameter $\varepsilon = k - 1 \ll 1$ is the closed-form expression

$$\begin{aligned}C_I(x) \approx &-\frac{1}{[2\pi(x - x_0)]^{1/2}} \\ &\times \left\{\left(1 - \frac{129/128}{(x - x_0)^2}\right)\sin\left(x - x_0 + \frac{\pi}{4}\right)\right. \\ &\left. - \frac{5/8}{x - x_0}\cos\left(x - x_0 + \frac{\pi}{4}\right)\right\}.\end{aligned} \tag{A19}$$

The coefficients of the higher-order terms in $(x - x_0)^{-1}$

are products of Taylor coefficients and values of the complete gamma function with parameters 3/2 and 5/2.

The full integral (A10) was evaluated numerically as described in G86. Some cases are shown here in Fig. 4. The maximum absolute value of the streamfunction, say ψ_m, always occurs downstream of the forcing point. In the barotropic solution with $z_f = \pi/4$ (Fig. 4a), we see that $\psi_m = -0.47$ about one unit downstream of the forcing. Setting $x - x_0 = 1$ and $z = z_0 = \pi/4$ in (A12) and neglecting C_G yields $\psi_G = -0.25$, or only about half of ψ_m. The estimate (A19) has a minimum value of $C_I = -0.22$, which shows that the rest of ψ_m is mostly due to the inertial waves. The first local extremum of the estimate (A19) occurs near $x = x_0 + 1.5$, slightly downstream of the actual streamfunction center for $z_0 = \pi/4$ in Fig. 4. For much lower forcing, (A19) significantly overestimates the inertial contribution to ψ_m, as the reflections begin to interfere. If $z < z_0 \ll 1$, the contribution from the reflections approximately multiplies (A18) by $2z_0^2$. Thus, the inertial wave contribution to the average horizontal velocity perturbation below the forcing, say $u'_{\text{avg}} = -\psi_m/z_0$, varies linearly with z_0 for shallow forcing.

The impact of the stationary waves upon the surface flow should depend sensitively on the height of the source because the vertical scale of the downward-propagating buoyancy modes is similar for a broad range of horizontal scales, and because the inertial wave train is always concentrated at the level of the forcing. Since C_I is independent of z_0 for high-level forcing, $z_0 \geq 1$, we expect the strongest wind perturbations to occur for $z_0 = O(1)$, except for the gravity wave contribution. This is consistent with the difference between $z_0 = \pi/4$ and $z_0 = \pi/2$ in the barotropic and cold-advection solutions. In the warm-advection solution, u'_{avg} is similar for these two forcing levels because of the enhanced baroclinic gravity wave contribution in the region $\beta(z - z_0) > 0$, as described by (A15).

b. Transient solution

We focus here on the region that separates steady waves from the overlying undisturbed flow. Background rotation will be neglected, as it will not qualitatively alter the dimensions of this wave front. The dispersion relation is then

$$(k - \nu)^2 m^2 - k^2 = 0. \tag{A20}$$

At the initial time, the wave front is a step function in z. For the single spectral component, $k_0 > 0$, the initial condition is $\psi = H(z)\cos(k_0 x + z)$, where $H(z)$ is the Heaviside function, or

$$\psi(x, z, 0) = \begin{cases} \cos(k_0 x + z), & z < 0 \\ 0, & z > 0. \end{cases} \tag{A21}$$

The choice $m = +1$, which is implicit in (A21), corresponds to upward energy propagation. The vertical transform is

$$\hat{\psi}(x, m, 0) = \frac{1}{4\pi i}\left(\frac{\exp(ik_0 x)}{m - 1_<} + \frac{\exp(-ik_0 x)}{m + 1_<}\right), \tag{A22}$$

where $1_<$ indicates that the poles are on the negative imaginary side of the real-m axis. Since upward energy propagation in general requires $\nu = \nu_+(k, m) = k - |k|/m$, the time-dependent solution is

$$\psi(x, z, t) = \frac{1}{4\pi i}\int_{-\infty}^{\infty}\left(\frac{\exp[ik_0(x - t)]}{m - 1_<} + \frac{\exp[-ik_0(x - t)]}{m + 1_<}\right) \times \exp\left[i\left(mz + \frac{k_0 t}{m}\right)\right] dm. \tag{A23}$$

As soon as $t > 0$, the m dependence of $\nu(k, m)$ prevents moving the complex integration path to $m = +\infty i$ to obtain the full solution in $z > 0$. Hence, a disturbance appears in $z > 0$. The boundary condition at $z = 0$ is maintained by (A23) because there is no downward signal propagation.

By defining $m' = m - 1$ or $m' = m + 1$ as necessary, the solution may be rewritten

$$\psi = \text{Re}\left\{\frac{\exp[i(k_0 x + z)]}{2\pi} \times \int_{-\infty}^{\infty}\exp\left[im'\left(z - \frac{k_0 t}{1 + m'}\right)\right]\frac{dm'}{im'}\right\}, \tag{A24}$$

where "Re" denotes the real part. We refer to the definite integral in (A24) as $I(z, t)$ and note that $I = 2\pi H(z)$ at $t = 0$, as required by (A21).

As an integral over m', $I(z, t)$ can be approximated for large z using the method of stationary phase (Bender and Orszag 1978). The phase $\varphi(m') = m'[z - k_0 t/(1 + m')]$ is stationary at $m' = \pm\sqrt{k_0 t/z} - 1$. The positive (negative) square root corresponds to upstream (downstream) intrinsic phase and group propagation. Since stationary modes have $m' = 0$, we can interpret

$$k_0 t \equiv z_1(t) \tag{A25}$$

as the height of a zero-frequency signal located initially at $z = 0$. At the stationary-phase points, we find that $\varphi = -(z^{1/2} \mp z_1^{1/2})^2$ and $d^2\varphi/dm'^2 = \pm 2z_1^{-1/2}z^{3/2}$. Hence,

$$\frac{dI}{dz} = \int_{-\infty}^{\infty}\exp\left[im'\left(z - \frac{k_0 t}{1 + m'}\right)\right] dm' \sim \sum_{\pm}\left(\frac{\pi^2 z_1}{z^3}\right)^{1/4}\exp\left[-i(z^{1/2} \mp z_1^{1/2})^2 \pm \frac{i\pi}{4}\right], \tag{A26}$$

where the sum is taken over the two stationary-phase points. Unfortunately, this estimate is not useful in $z <$

z_1 because of the constraint $z^3 \gg z_1$ implicit in the approximation method.

If we write $z = z_1(t) + z'$, then z' is the vertical coordinate in a frame moving vertically with the energy of the stationary waves. With $z' \ll z$, the phase in (A23) is $\varphi \approx -z'^2/4z_1$ for the part of the disturbance originating from below the observation point and $\varphi \approx 4z_1 + 2z'$ for the part originating from upstream. Over isolated topography, the latter is removed by horizontal dispersion. Hence the modification of the steady wave field above the forcing includes a gradual phase modulation on the scale $\sqrt{z_1(t)}$.

The last result can be obtained independently by assuming that the integral is dominated by nearly stationary waves, $m' \approx 0$. Using a truncated Taylor series for $\varphi(m')$ about this value yields

$$\frac{dI}{dz} \sim \int_{-\infty}^{\infty} \exp[im'(z - z_1) + iz_1 m'^2]\, dm' = \left(\frac{\pi}{z_1}\right)^{1/2} \exp\left[-i\left(\frac{z - z_1}{2z_1^{1/2}}\right)^2 + \frac{i\pi}{4}\right]. \quad \text{(A27)}$$

This gives the same result near $z = z_1$ as (A26). The variation of amplitude away from $z = z_1$ is not provided by (A27), and (A26) is not valid in $z < z_1$. However, the scale of the wave front can be inferred from the amplitude of the jump. Thus, if $dI/dz \sim z_1^{-1/2}$, then $dz \sim z_1^{1/2}$ is necessary to preserve an $O(1)$ variation in $I(z, t)$.

Assume that the disturbance over the mountain consists of steady waves near the surface, separated from an overlying, undisturbed region by a transition layer of depth h_f and height z_f. The estimate for $F^{(u)}$ becomes $\mathrm{Fr}h_f^{-1}$ times the steady momentum flux, $u_0 w_0$, which is of order Ro. The nonlinearity in the transient problem for ψ_1 is $F_A = (\partial_x + \partial_t)F_z^{(u)}$. Hence, the volume integral is of order $\mathrm{FrRo}h_f^{-1}(1 + l_f/\tau_f)$, where l and τ denote horizontal distance and Eulerian timescales in the transition layer. Signals rise at the vertical group speed,

$$c_{gz} = -km^{-2}(1 + m^2/k^2)^{-1/2}. \quad \text{(A28)}$$

Since $k \approx \mathrm{Ro} \geq O(1)$ and $m \approx 1$ at the bottom of the layer, (A28) implies that $c_{gz} \sim k \sim \mathrm{Ro}$. Thus, since $(l_f/\tau_f) \sim k^{-1}(c_{gz}/h_f) \sim h_f^{-1}$, the largest part of the momentum forcing when $h_f < 1$ is $\mathrm{FrRo}h_f^{-2}$.

Comparing this result to the estimate in section 3 for steady momentum forcing (namely FrRo^{-1}), and assuming $\mathrm{Ro} > 1$, we see that the transient forcing ceases to be important when the depth h_f is of order $\mathrm{Ro}^{3/2}$. However, for large z and t in the case of an impulsive startup, the stationary-phase arguments indicate that $h_f \sim \mathrm{Ro}z_f^{1/2} \sim \mathrm{Ro}^{3/2}t^{1/2}$. This means that the transient momentum forcing becomes unimportant for $t > O(\mathrm{Ro})$. The actual surface wind, $u = -\psi_z$, induced by the transient forcing is further diminished by a factor of $z_f^{-1/2}$ or z_f^{-1} for large z_f.

REFERENCES

Bender, C. M., and S. A. Orszag, 1978: Asymptotic expansion of integrals. *Advanced Mathematics for Scientists and Engineers,* R. Ciofalo, Ed., McGraw-Hill, 247–316.

Bretherton, C., 1988: Group velocity and the linear response of stratified fluids to internal heat or mass sources. *J. Atmos. Sci.,* **45,** 81–93.

Garner, S. T., 1986: An orographic mechanism for rapid frontogenesis. Ph.D. dissertation, Massachusetts Institute of Technology, 222 pp. [Available from MIT, 77 Massachusetts Ave., Cambridge, MA 02139-4307.]

——, 1995: Permanent and transient upstream effects in nonlinear stratified flow over a ridge. *J. Atmos. Sci.,* **52,** 227–246.

——, 1999: Blocking and frontogenesis by two-dimensional terrain in baroclinic flow. Part I: Numerical experiments. *J. Atmos. Sci.,* **56,** 1495–1508.

Ley, B. E., and W. R. Peltier, 1978: Wave generation through frontal collapse. *J. Atmos. Sci.,* **35,** 3–17.

Lighthill, M. J., 1952: On sound generated aerodynamically. I. General theory. *Proc. Roy. Soc. London,* **211A,** 564–587.

Lilly, D. K., and J. B. Klemp, 1977: The effects of terrain shape on nonlinear hydrostatic mountain waves. *J. Fluid Mech.,* **95,** 241–261.

Long, R. R., 1953: Some aspects of the flow of stratified fluids, I. A theoretical investigation. *Tellus,* **5,** 42–48.

McIntyre, M. E., 1972: On Long's hypothesis of no upstream influence in uniformly stratified or rotating flow. *J. Fluid Mech.,* **52,** 209–243.

Pierrehumbert, R. T., 1984: Linear results on the barrier effect of mesoscale mountains. *J. Atmos. Sci.,* **41,** 1356–1367.

——, 1985: Stratified semi-geostrophic flow over two-dimensional topography in an unbounded atmosphere. *J. Atmos. Sci.,* **42,** 523–526.

——, and B. Wyman, 1985: Upstream effects of mesoscale mountains. *J. Atmos. Sci.,* **42,** 977–1003.

Queney, P., 1947: Theory of perturbations in stratified currents with application to airflow over mountain barriers. Misc. Rep. 23, Dept. of Meteorology, University of Chicago, 67 pp. [Available from University of Chicago, 5801 South Ellis, Chicago, IL 60637.]

Segur, H., 1973: The Korteweg–de Vries equation and water waves. Solutions of the equation. Part 1. *J. Fluid Mech.,* **59,** 721–736.

Smith, R. B., 1977: The steepening of hydrostatic mountain waves. *J. Atmos. Sci.,* **34,** 1634–1654.